Experimental Investigation of 193-nm Laser Breakdown in Air

Magesh Thiyagarajan, *Member, IEEE*, and John E. Scharer, *Senior Member, IEEE*

Abstract—We present the measurements and analysis of laser-induced breakdown processes in dry air at a wavelength of 193 nm by focusing 180-mJ 10-MW high-power 193-nm UV ArF laser radiation onto a 30-μm-radius spot size. We examine pressures ranging from 40 torr to 5 atm, for laser power densities of 1 TW/cm^2, well above the threshold power flux for air ionization. The breakdown threshold electric field is measured and compared with classical and quantum theoretical ionization models at this short wavelength. A universal scaling analysis of these results allows one to predict aspects of high-power microwave breakdown based on measured laser breakdown observations. Comparison of 193-nm laser-induced effective field intensities for air breakdown data calculated based on the collisional cascade and multiphoton breakdown theories is used successfully to determine the collisional microwave scaled portion with good agreement regarding both pressure dependence and breakdown threshold electric fields. Using a laser shadowgraphy diagnostic technique, the plasma and shock-wave dynamics are analyzed. Blast shock-wave expansion of the plasma and laser-heated neutral gas is observed with average velocities of 47 km/s, and the temporal shock-wave velocity variation is used to determine electron temperature evolution just behind the shock wave.

Index Terms—Air plasma, breakdown scaling, excimer laser, laser-induced plasma, shadowgraphy.

I. INTRODUCTION

THERE IS a great deal of research and industrial interest in laser-induced plasmas, and the range of applications involving plasmas produced by lasers spans a large domain within science and technology. Laser-produced plasmas are widely used in laser ablation, micromachining, laser fusion, and laser-initiated switching applications [1]–[4]. The laser-induced gas breakdown experiments using infrared and optical wavelength lasers have been summarized by Raizer [3]. Due to continued development of lasers with high powers and shorter wavelengths, there has been steady interest in the laser-induced breakdown plasmas. This paper examines the ionization process at shorter wavelengths than have been examined previously where quantum multiphoton processes play a significant role.

Laser-induced breakdown can be defined as the generation of an ionized gas or plasma during or by the end of the pulse. The experimental criterion that is generally used is the observation of a glow or flash in the focal region for 10%–50% of the laser firings. As described by Raizer [3], the photon-initiated electron cascading plasma process begins when a pulsed laser beam is focused down to a small spatial domain, which produces a very sudden temperature rise in the medium at that point. If the electric field of the laser radiation near the focus becomes greater than that of the binding electrons to their nuclei, it will trigger breakdown of the air molecules and produce ionization of the gas. This breakdown causes a cascade effect because the increasing plasma density becomes very absorbent to the laser so that more of the energy is absorbed. At first, primary and secondary electrons are created through the rising phase of the laser pulse by several mechanisms, namely, free electrons in the air at room temperatures, multiphoton ionization (MPI) [5]–[7], and the inverse bremsstrahlung absorption or cascade ionization process, which corresponds to an ionizing collisional cascade (CC) evolution [4], [8].

These two ionization mechanisms differ fundamentally and are described by different theories that are required to interpret these new experiments at 193 nm where the laser photon energy is $\varepsilon_\gamma = 6.4$ eV. For the MPI process, a neutral atom absorbs enough laser photons within a quantum lifetime of the excited state [6] [$\tau = h/\varepsilon_\gamma = 6.56 \times 10^{-16}$ s (at 193 nm)] to raise it from the ground state to the ionization level or above. If enough atoms are ionized, it may also produce an observable spark [6]. For a cascade ionization process, a few initial electrons in the breakdown region are required, which could be created by a process such as MPI of the gas species or the presence of dust or the creation of electrons at the ambient gas temperature. These electrons then gain energy by absorbing laser energy and undergoing elastic collisions with neutral atoms. After accumulating an energy slightly higher than the ionization potential of the gas, the electron may ionize an atom by inelastic collisions producing two electrons of low energy; these are then available for the process to be repeated [8].

Pioneering experiments on measuring optical breakdown thresholds for air using a high-power optical ruby laser were carried out by Meyerand and Haught in 1963 [2], [4]. More recent experiments were conducted at infrared and visible wavelengths of the high-power lasers available: 385 μm(D$_2$O), 10.6 μm(CO$_2$), 3.8 μm(DF), 2.7 μm(HF), 1.06 μm(Nd:Yag), and 0.69 μm(Rb) [3]. Emphasis in more recent years has been on short-wavelength excimer lasers such as 0.25 μm(XeF) and 0.25 μm(KrF) [1]. However, to our knowledge, no research has been carried out to date on the breakdown threshold and

plasma formation measurements for air using an ultraviolet excimer laser radiation at 193 nm (ArF) that can have substantial multiphoton processes contributing to the ionization.

The photon energies ($\varepsilon_\gamma = 1.24/\lambda$, where λ is the vacuum wavelength in micrometers) of the infrared and visible laser radiation experiments used until now ($385-0.69$ μm) [3] are well below the ionization energy of air (15.6 eV), and thus, it requires 10–300 photons to be absorbed within a quantum lifetime of the excited state on the order of $< 10^{-14}$ s, which is highly improbable to occur [6], [8]. Therefore, in the earlier air breakdown experiments [3] using infrared and visible lasers, the ionization mechanism is primarily due to cascade ionization with negligible or no MPI. However, in the ultraviolet regime, particularly for our experimental case of ArF excimer ultraviolet laser radiation at 193 nm (6.4 eV), wavelength requires only three photons to be absorbed within a short quantum excitation lifetime [6] (within a time $\tau \approx h/\varepsilon_\gamma = 6.5 \times 10^{-16}$ s) in order to ionize the air molecules. Therefore, MPI processes should play a significant role in our air breakdown experiments along with the competing cascade ionization processes. In general, the cascade theory best describes the breakdown at high pressures (> 100 torr) and long laser pulse lengths (> 10 ns) [8]. On the other hand, the MPI theory alone should best describe the breakdown at lower pressures, in the millitorr regime where the electrons are more collision less, and for short pulse lengths (< 1 ns) [6] where the cascade process cannot develop. Our experiments are in the mixed region where both processes must be considered.

In this paper, we report measurements and analysis of air breakdown processes by focusing our 193-nm 180-mJ 10-MW high-power UV laser radiation onto a 30-μm-radius spot size ($r = f\alpha/2$, where $f = 2$ cm is the focal length and $\alpha = 3$ mrad is our laser beam divergence) that produces laser power densities up to $\geq 10^{12}$ W/cm^2, well above the CC threshold power flux for air ionization at this wavelength that is 10^{10} W/cm^2 [9]. The breakdown threshold is measured and compared utilizing classical [10] and quantum theoretical ionization models [5], [6].

In addition, our investigation of the breakdown threshold field intensities for air using ArF 193-nm laser radiation is extended to correlate the corresponding [10], [11] threshold field requirements by using high-power microwave radiation by means of "universal plot" [10], [11]. A universal scaling analysis of these results allows one to predict aspects of high-power microwave air breakdown based on measured laser breakdown observations. The high-power microwave breakdown threshold has been investigated experimentally [12]–[14] and computationally [15], [16].

The characteristics of the laser-induced plasma are diagnosed using optical diagnostics. The laser energy absorbed by the plasma and the laser energy transmitted through the plasma are measured using a calibrated laser energy detector, and the results are described. We have also applied the plasma shadowgraphy technique [17] using a fast-gating imaging technique for visualizing the laser-induced gas-dynamic processes of the laser-induced plasma. Shadowgraphy measurements in and near the focus can shed light on typical postbreakdown effects. Using this technique, one can measure the velocity of

plasma expansion and the laser-heated neutral density shock wave immediately after the breakdown. The temperature behind the expanding plasma and the shock wave is measured by determination of the expansion velocities, using Zeldovich's [18] tabulated flow quantities, primarily the temperature just behind a shock-wave front in air with standard conditions ahead of the wave ($p_0 = 1$ atm and $T_0 = 293$ °K). This theory is based on the Hugoniot curve's [18, p. 209] neutral density ratio at the front of the shock wave relative to that just behind the shock front, specific heat with the effect of dissociation and ionization included in processes behind the shock wave. The experimental system and diagnostics are presented in Section II, experimental results are discussed in Section III, and a summary is presented in Section IV.

II. EXPERIMENT

A. Excimer-Laser-Induced Plasma System

The schematic diagram of the experimental setup is shown in Fig. 1. In this experiment, a pulsed 193-nm excimer laser (Lumonics, Pulsemaster PM-842, Argon Fluoride, $\lambda = 193$ nm, 6.4 eV per photon) that runs with a gas mixture containing 5% F_2 in Ar was operated shot by shot. The laser output is a rectangular beam of 2.8×1.2-cm cross section with homogeneous ($\pm 5\%$) beam intensity. The full-width at half-maximum (FWHM) of the laser pulse is 20 ± 2 ns, with a 2-ns rise/fall time and a maximum available laser output energy of 200 mJ. A typical working output of up to 180 ± 5 mJ is used in the experiment.

The rectangular cross section of the laser beam was reduced to 1 cm $\times$ 1 cm using a set of 193-nm coated cylindrical Suprasil planoconvex and cylindrical planoconcave ($f = 10$ cm and $d = 5$ cm) UV fused silica lenses to more closely match the 1-cm-diameter objective focus input lens. In this experiment, all UV optical components are specially coated, with 98% transparency at 193 nm. The laser energy passing through the cylindrical lenses is measured using laser energy meters (Scientech, AC 50 UV Calorimeter and Astral, AD30 Laser Energy Meter).

The laser beam enters the plasma chamber through a 193-nm transmission coated 3-cm-diameter Suprasil UV quartz window. The laser beam was focused by using a high-power handling (100-MW/cm^2) objective lens mounted inside the plasma chamber. The objective lens (OFR, LMU-10X-193) has an effective focal length of 20 mm, with a 10-mm entrance aperture and a 0.25 NA. Due to its short focal length, the objective lens is mounted inside the plasma chamber using an adjustable length holder, so that the laser-induced plasma will be positioned on the cylindrical chamber axis. The space between the entrance UV window and the objective lens is maintained at the same pressure as that of the chamber pressure in order to avoid differential pressures acting on the objective lens. Great care was taken to position the objective lens together with the plasma chamber precisely in the line of sight with the UV laser beam for the air breakdown experiments.

Following the 1-cm $\times$ 1-cm reduced-size laser beam from the planoconcave lens, the objective focus lens uses only the center 1-cm-diameter circular portion, and the excess portion around
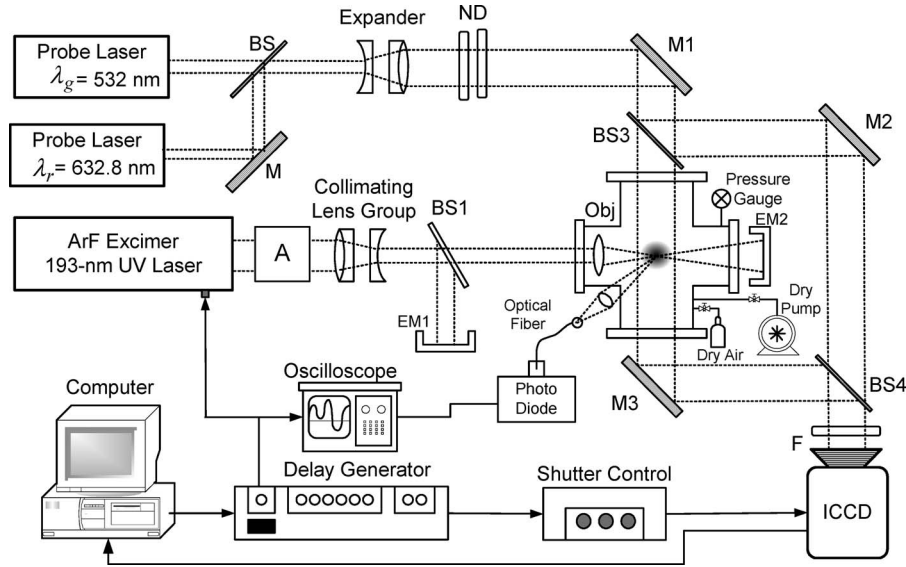
Fig. 1.   Schematic of the experimental and diagnostic setup of 193-nm laser-induced plasma. A—Attenuator. BS—Beam Splitter. EM—Energy Meter. Obj—Objective Lens. M—Mirror. F—Filter. ND—Neutral Density Filter.

the edges of the beam is eliminated. By eliminating the edges of the laser beam, edge effects that could affect the focus of the uniform laser beam are minimized. Utilizing this technique, 21% of the laser output beam's energy is measured to be lost. In addition, it is found that the laser beam experiences a 6% loss as it passes through the coated UV optics, including the cylindrical planoconvex/concave lenses, a Suprasil UV quartz window, and the objective focal lens. These results are obtained using a laser energy meter (Scientech, AC 50 UV Calorimeter and Astral, AD30 Laser Energy Meter). The laser energy available immediately after the objective lens corresponding to a 180 ± 5-mJ laser output was measured by the Scientech energy meter to be 135 ± 5 mJ, corresponding to the measured incident laser energy on the focal spot, in agreement with the analytical estimate.

The plasma chamber was made from stainless steel and was designed to hold pressures from 10 mtorr to 6 atm (4560 torr). Optical view ports on both sides of the cell are made of 3-cm-diameter by 5-mm-thick sapphire windows to withstand pressures up to 6 atm. The view ports enabled observation of the interior at right angles to the cell axis which is coincident with the direction of the laser beam, as well as for diagnosing the plasma. The chamber was evacuated with a dry scroll pump (Varian, SH-110) down to 10 mtorr and flushed several times before finally filling with dry air (< 10-ppm water) to the desired pressure. The chamber pressure was measured precisely by two pressure gauges, namely, a MicroPirani vacuum gauge with a pressure controller–readout (MKS Instruments, 910-11 and PDR 900-11) to measure pressure ranges from 10 mtorr to 1500 torr and a high-pressure digital pressure gauge (GE, Druck DPI 104) capable of measuring pressure ranges from 760 torr to 10 atm. The gas flow through the chamber was regulated by a needle valve in the gas line and another valve in the pumping line. For one set of experiments on determining the effects of removing microdust particles of diameters ≥ 0.1 μm on the breakdown threshold of dry air, we have inserted a filter capsule in the incoming gas line and cleaned residual dust on window

and lens surfaces by means of an aerosol jet. The filter houses a dual-pleated polytetrafluoroethylene (PTFE) filtering element with $\leq 0.1-\mu$m pore size.

B. Theoretical Breakdown Threshold Estimation

The breakdown threshold based on the quantum MPI processes is derived by Nelson [5], [19]. In MPI, a neutral atom absorbs enough laser photons in a short time to raise it from the ground state to the ionization level or above. If enough atoms are ionized, it may produce a visible spark [8]. The interaction threshold I_0 is written in terms of flux density as

$$I_0 = h v_1 c N_0 \tag{1}$$

with $N_0 = 2(2\pi)^3 \times 137 \times (1/\lambda)^3$. Therefore, the breakdown threshold can be defined as

$$I_{B(\mathrm{MPI})} = S I_0 \tag{2}$$

where S is the MPI coefficient, which is the ratio of ionization potential, U_i, of the gas (15.6 eV for air) [10], [11], [20] to the photon energy, ε_γ, of the laser beam. With 6.4-eV photon energy for the 193-nm laser radiation, it requires $S = 3$ photons to be absorbed within the quantum excitation lifetime $\tau \approx h/\varepsilon_\gamma = 6.5 \times 10^{-16}$ s [6] in order to ionize the air molecules. Thus, the intensity threshold value for 760-torr air at 193-nm laser radiation is $I_B = 8.7 \times 10^{11}$ W/cm^2. The corresponding rms breakdown electric field is obtained from

$$E_{B(\mathrm{MPI})} = 1.94 \times 10^4 \sqrt{I_B} \tag{3}$$

and we obtain $E_{B(\mathrm{MPI})} = 18 \times 10^6$ V/cm, where I_B is expressed in megawatts per square centimeter. Thus, our experiment can substantially examine the effects of MPI processes at 193 nm that are important for lower pressure air plasmas.

Kroll and Watson [6] have reviewed the theory of CC ionization phenomena in air, based on the data obtained by

MacDonald [10]. In the cascade ionization process, a few initial free electrons are assumed to be present in the focal region, and these electrons then gain energy by absorbing laser energy upon elastic collisions with neutral atoms. After a cascade that accumulates an energy slightly higher than the ionization potential of the gas, the electron may ionize an atom by inelastic collisions producing two electrons of low energy; these are then subjected to the collisional process and are repeated. If enough atoms are ionized within the laser pulse period, breakdown is observed as a bright spark. Based on this theory, the threshold power flux for breakdown is given by [6]

$$I_{B(\mathrm{CC})} = 1.44 \times 10^6 (p^2 + 2.2 \times 10^5 \lambda^{-2}) \ \mathrm{W/cm^2} \quad (4)$$

where p is the pressure in atmospheric pressure units and λ is the radiation wavelength in micrometers. Although this theory is primarily based on observations at microwave frequencies, and as well as pressures below atmospheric conditions, it has also been scaled to longer 1.06-μm-wavelength Nd:YAG laser frequencies and higher pressures [11]. The cascade ionization theory predicts a breakdown flux intensity threshold value for our 193-nm wavelength of $I_{B(\mathrm{CC})} = 8.5 \times 10^{12} \ \mathrm{W/cm^2}$ corresponding to $E_{B(\mathrm{CC})} = 56 \times 10^6 \ \mathrm{V/cm}$, assuming that there are no dust particles ($r \sim 1$–$2 \ \mu$m) nor significant water vapor in the air.

C. Shadowgraphy Diagnostic

In a plasma, the refractive index is primarily a function of the electron density, which is the main plasma parameter determined by refractive-index measurements. Typical plasma diagnostics based on refractive effects include interferometry, Schlieren imaging, shadowgraphy, and Faraday rotation measurements [17]. While the first technique gives a direct measure of the refractive index μ, the Schlieren and shadowgraphy techniques probe the refractive-index gradient $d\mu/dx$. In this experiment, the shadowgraphy technique is applied for visualizing the laser-induced plasma and laser-heated gas dynamic processes. In general, a shadowgraph is a measure of the displacement of light rays as they pass through a medium. An electromagnetic wave exerts a force on the charged constituents of the medium through which it propagates. This force accelerates the charges which, in turn, modify the time-varying electromagnetic field. A solution of an electromagnetic-wave propagation in a plasma can be obtained by solving the wave equation for a plane wave in the small amplitude approximation [8]. The plasma refractive index then follows as

$$\mu = \left(1 - \frac{\omega_p^2}{\omega^2 (1 \pm \omega_e/\omega) \left[1 - (\nu/\omega)\right]} \right)^{1/2} \quad (5)$$

where $\omega = 2\pi c/\lambda$ is the frequency of the electromagnetic wave. In our case, $\lambda = 532$ nm, and there is no dc magnetic field ($\omega_e = 0$). The electron plasma frequency is $\omega_p = (n_e e^2/\varepsilon_0 m_e)^{1/2}$, and ν is the effective number of collisions per second that an electron makes with neutrals.

In our case, where $\nu/\omega \ll 1$, the collision rate in atmospheric (760 torr) air plasma is on the order of 10^{11} Hz [21] and
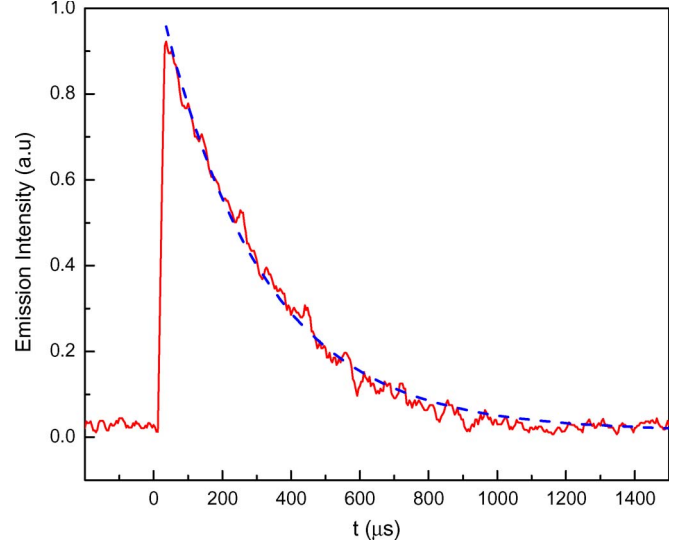

Fig. 2. Temporal evolution of total detector intensity from emission of laser-induced plasma in air.

negligible compared to ω, and therefore, (5) simplifies to

$$\mu_{\mathrm{electrons}} = \sqrt{1 - \frac{\omega_p^2}{\omega^2}} = \sqrt{1 - \frac{n_e}{n_c}} \quad (6)$$

where

$$n_c = \frac{4\pi^2 c^2 \varepsilon_0 m_e}{e^2 \lambda^2} = \frac{\pi}{r_e \lambda^2} \quad (7)$$

is the cutoff density and $r_e = e^2/(4\pi\varepsilon_0 m_e c^2) = 2.818 \times 10^{-15}$ m is the classical electron radius. In our shadowgraphy experiments, as shown in Fig. 1, a green laser at $\lambda = 532$ nm is used as a light source due to its coherence, brightness, and narrow bandwidth. The cutoff density for 532 nm is 3.9×10^{21} cm^{-3}, which is well above the densities encountered in our laser-focused plasma experiments.

III. EXPERIMENTAL MEASUREMENTS, RESULTS, AND DISCUSSION

A. Breakdown Threshold Measurements

Breakdown threshold is defined as the lower laser intensity at which a visible spark is obtained [11]. In this paper, the definition of breakdown threshold used is that flux which produces air breakdown for 50% of the laser pulses. The occurrence of breakdown was determined by observing a visible spark at a right angle to the laser beam direction using a high-speed (< 2-ns rise time) visible photodetector (Thorlabs, DET10A/M) while gradually increasing the intensity for each laser pulse. Fig. 2 shows the temporal decay of the total light emission intensity from the laser-induced plasma, in which the time zero ($t = 0$) is taken as the beginning of the laser pulse.

The measurements were made in dry air (< 10-ppm water) at room temperature. The primary measurement is the incoming laser energy with the corresponding intensity at the focal spot and is then calculated. In this paper, the focal length f
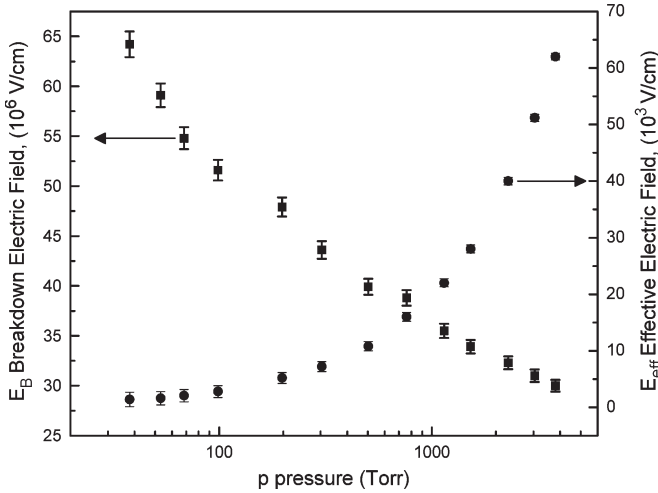
Fig. 3. Measured breakdown threshold electric field E_B and effective electric field E_{eff} plotted as a function of pressure p in torr.

of the objective lens used is 2.0 cm, and the width w_b of the unfocused laser beam used is 1.0 cm, with a laser beam divergence α of 3.0 mrad. Following standard optical focal theory, the minimum focal volume is assumed to be cylindrical [11] with a corresponding radius of $r = f\alpha/2 = 30$ μm and an axial length (depth of focus) of $l = 0.414(\alpha/w_b)f^2 = 120$ μm. The characteristic diffusion length is obtained by [10], [11], [22]

$$\left(\frac{1}{\Lambda}\right)^2 = \left(\frac{\pi}{l_0}\right)^2 + \left(\frac{2.40}{r_0}\right)^2 \tag{8}$$

which yields a value of $\Lambda = 12$ μm. This value for plasma diffusion length is close to the $2r_0/6 - (\mu\text{m})$ value used in previous longer wavelength (10.6-μm) air breakdown laser experiments [23]. Another aspect when comparing the pulsed 193-nm laser breakdown data to the steady-state continuous-wave (CW) microwave breakdown case is that, although the laser energy is pulsed (20 ns), there are many oscillations ($> 3 \times 10^7$ cycles) in the electric field within a single pulse. The threshold breakdown in air using a focused laser radiation is independent of pulse length and can be treated as if in steady state if the number of cycles contained within the pulse is more than 10^6 [11].

The breakdown threshold laser intensity at the focal minimum is determined by

$$I_B = \frac{1}{\pi}\left(\frac{W_B}{r_0^2 \tau_p}\right) \tag{9}$$

where W_B is the minimum laser pulse energy at which the breakdown is observed, r_0 is the focal spot radius, and τ_p is the FWHM of the laser pulse. From I_B, the breakdown threshold electric field E_B is determined using $E_B = 1.94 \times 10^4 \sqrt{I_B}$. In our experiment, we have measured the breakdown threshold for air at pressures ranging from 40 to 3800 torr (5 atm). In Fig. 3, the solid squares show the measured breakdown electric field in air for various pressures. The E_B value for dry air at 760 torr was measured to be 38×10^6 V/cm, and it is observed

that E_B decreases for pressures ranging from 40 torr to 5 atm, which is expected in our regime where the laser frequency ω is much higher than the electron collision frequency $v_c(\omega \gg v_c)$. It indicates that for such high-frequency wave fields, there are many oscillations of the electric field per collision. It is therefore convenient to make use of the concept of effective electric field for energy transfer. The effective electric field appears in the form [10], [11]

$$E_{\text{eff}} = E_B \left(\frac{v_c^2}{v_c^2 + \omega^2}\right)^{1/2}. \tag{10}$$

The effective electric field represents the effectiveness of the electric field in coupling its energy to the electron with the field multiplied by the factor $(v_c^2/(v_c^2 + \omega^2))^{1/2}$. For our experimental conditions, $\omega/v_c \gg 1$, and thus

$$E_{\text{eff}} \approx E_B \left(\frac{v_c}{\omega}\right). \tag{11}$$

The electron collision frequency is determined by $v_c = \beta \times 10^9 p$, where p is in torr. The parameter β depends on the gas used, with a value of 5.33 for air data [10], [11], [20]. The effective electric field E_{eff} is shown in Fig. 3 (circles) as a function of pressures ranging from 40 torr to 5 atm, and it is observed to increase within the pressure range, which means that the effectiveness of energy coupling through electron collisions is higher above atmospheric pressures when compared to partial vacuum conditions. It has been observed that, at 1.06-μm laser wavelengths, for gas pressures above 50 torr and pulse lengths in the 10^{-9}-s range, gas breakdown is best described by the cascade ionization processes [8]. However, at 193-nm laser wavelength laser radiation with the higher photon energy (6.4 eV), we find that MPI processes play a significant role even for pressures higher than 50 torr.

Using this concept of effective electric field, the comparison of 1.06-μm laser-induced breakdown data for air with scaled calculations based on the CC theory was done effectively when compared with microwave data and shows good agreement [11]. The laser-induced breakdown data are effectively compared with the microwave data using a universal plot that has $E_{\text{eff}}\Lambda$ as the ordinate plotted as a function of $p\Lambda$. The 2-D universal plot represents all four laser breakdown parameters including pressure, frequency, diffusion length, and electric field.

In Fig. 4, the experimental values of $E_{\text{eff}}\Lambda$ obtained from our measured dry-air (without any gas filter) breakdown data are compared with typical microwave CW data for air shown in solid line curve. The dashed curve shows the classical cascade breakdown theory (4) extended to 193-nm laser radiation wavelength. According to this theoretical result, the breakdown threshold for air at 193-nm-wavelength radiation converges with the microwave breakdown data at above atmospheric pressures and deviates significantly for very low pressures. However, for low pressures, the medium becomes less collisional, and the MPI process will dominate over the collisional breakdown process, although the MPI process is a weak function of pressure ($p^{-1/3}$) [22]. In Fig. 4, the triangles show the measured breakdown data for air from 40 torr to 5 atm. In order
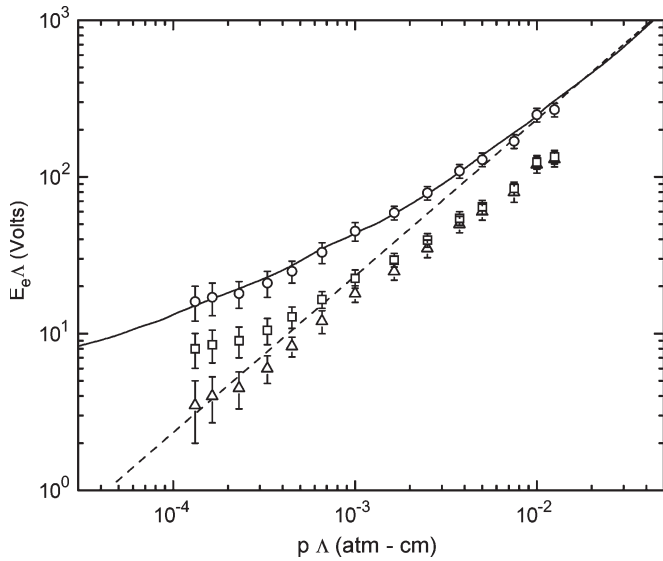
Fig. 4. Universal plot of (triangles) experimental 193-nm laser breakdown threshold fields in dry air (without gas filter) compared with (solid line) microwave theory. (Dotted line) Microwave theory extended to $\lambda = 193$ nm. (Squares) MPI-corrected breakdown threshold data. (Circles) Data in squares scaled by a factor of 1.95.
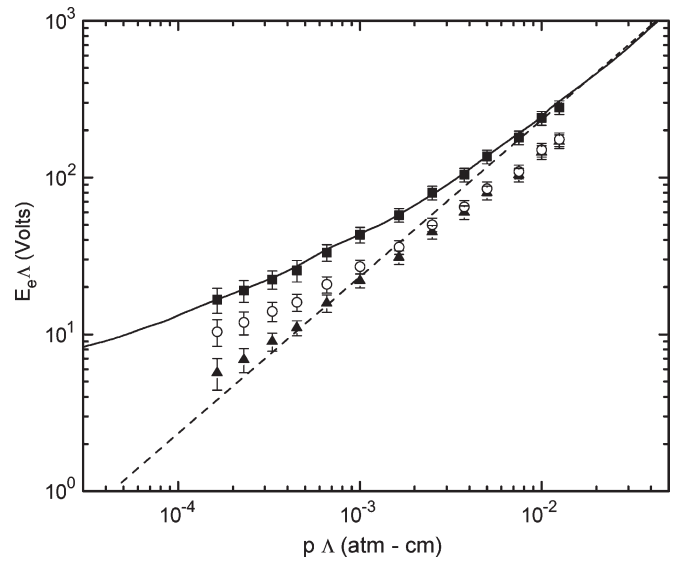
Fig. 5. Universal plot of (triangles) experimental 193-nm laser breakdown threshold fields in dry air (with 0.1-μm filter) compared with (solid line) microwave theory. (Dotted line) Microwave theory extended to $\lambda = 193$ nm. (Circles) MPI-corrected measured breakdown threshold (triangles) data. (Squares) Data in circles scaled by a factor of 1.51 to yield square values.

to compare it with the collisional microwave breakdown, the 193-nm laser-induced breakdown data, where MPI processes play a role at lower pressures, a correction for the MPI process as a function of pressure is necessary. From the measured breakdown data, the portion of MPI effects as a function of pressure $p^{-1/3}$ is eliminated by correcting with a multiplicative factor $E_B \times [(E_{B(CC)}(p) + E_{B(MPI)}(p))/E_{B(CC)}(p)]$, where the terms are given by (3) and (4) as a function of pressure, and the results are shown by squares in Fig. 4. The corrected CC data shift to a much higher value at lower pressures where the MPI process is significant compared to that in higher pressures where collisional processes dominate. This means that a higher electric field is required in order to obtain breakdown at lower pressures without the influence of MPI processes. The breakdown threshold values were then multiplied by a scaling factor of 1.95 in order to scale with the microwave breakdown plot to examine the overall trend of the data as pressure is varied. The scaled data are shown by circles in Fig. 4. Similar scaling values were used in 1.06-μm laser breakdown experiment, where quantum multiphoton effects were negligible, in order to compare the scaled results with microwave breakdown data. For laser-induced breakdown in air at $\lambda = 1.06$ μ [11], the measured data were scaled by a factor of 2.24 in order to fit the microwave breakdown data.

Our 1.95 scaling factor can also be due to the fact that larger spatial wavelength averages of the microwave breakdown data are on the order of several centimeters, whereas the localized laser focus diameter is 60 μm. Another possibility for the factor is the presence of microscopic dust particles on the order of several micrometers in size, which has been shown to reduce breakdown for short-wavelength lasers but does not influence the longer wavelength microwave breakdown [23]. In order to investigate the effect of dust on the breakdown threshold, consequently, on the scaling factor, we have carried out a set

of similar breakdown threshold measurements with a 0.1-μm dual-pleated PTFE filter inserted in the incoming gas pipeline. In laboratory air, the average size of dust particles is about 1–2-μm diameter [23], and therefore, filtering dust particles of 0.1 μm or larger diameter will rid our system of them if present. We also sprayed the windows and objective lenses with a laser cleaning aerosol jet to eliminate dust formation from the laser flux on the optical surfaces. The result of the breakdown threshold measurements as a function of pressure range from 90 torr to 5 atm is shown in Fig. 5.

With the filter present, the minimum pressure at which the breakdown was observed at 135-mJ UV laser flux is 90 torr, whereas without the filter, the minimum breakdown pressure is 40 torr. As expected, the breakdown threshold for dry air as a function of pressure increases somewhat at lower pressures with the 0.1-μm filter. After correcting for the MPI process from the measured breakdown threshold values (triangles) that are then given by circles, we then multiply the result by a scaling factor of 1.51 in order to fit the measured data with the microwave breakdown curve, as shown in solid squares. It is evident that the presence of dust particles does play a role in the breakdown threshold values at lower pressures, as observed in our case. The scaling factor can also be attributed to the wide differences in frequencies between the microwave and laser frequencies ($\sim 5 \times 10^5$ Hz). The resulting UV laser pressure scaling agrees well with the average microwave curve. In our experiment, the overall pressure variation of the scaled data is in good agreement with the classical microwave breakdown results. It should also be noted that the microwave cascade curve is an average and subject to a range variation about the plotted values. The important aspect is that the pressure scaling of laser and microwave cases is similar over a wide range of pressures, as well as at lower pressures where a correction of the MPI process is required.
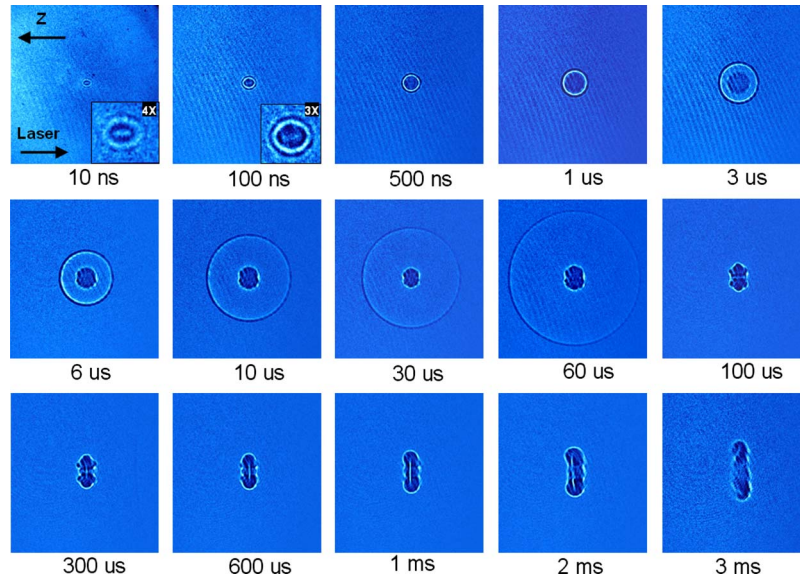
Fig. 6.   Shadowgrams of the 193-nm laser-focused plasma in air, with laser input radiation of 135-mJ energy. Each image has a spatial extent of 1.3 cm. The gating time for each image is 10 ns.

B. Excimer Laser—Output, Incident, Transmitted, and Absorbed Energy

As noted earlier, the 193-nm excimer laser has a maximum output of 200 mJ and a 20 ± 2-ns FWHM with a 2-ns rise/fall time. A stable working output energy of 180 ± 5 mJ is maintained throughout the experiment. While removing the edges of the square laser beam, 21% of the laser energy is lost, and there is a 6% loss of the laser output energy while passing through the UV focusing optics. The losses are determined by placing the individual UV optics in the laser beam path, and the transmitted energy was measured using the Astral energy meter.

With the UV focusing optics in place, a laser energy of 135 ± 5 mJ was measured immediately after the objective lens by placing the laser energy detector surface in contact with the output edge of the objective lens where the laser intensity is not sufficiently high to damage the detector. Therefore, a laser energy of 135 ± 5 mJ was incident and focused onto the 30-μm-radius spot size. This transmitted energy level is used as a reference level for all additional measurements.

A luminous plasma was observed for all 180-mJ laser pulses at the focal spot, 20 mm from the edge of the objective lens. In order to measure the transmitted energy through the plasma, the 5-cm-diameter sensor energy meter was placed 20 mm after the focal spot, where the transmitted laser energy can be measured. Since the maximum plasma frequency divided by the laser frequency near the focal spot is $\omega_p/\omega \sim 0.01$ at plasma densities of $\sim 10^{18}/cm^3$, we assume that very small fraction of the incident laser flux is scattered at large angles by the plasma, and the laser absorption is primarily due to CC and MPI processes. An average transmitted energy of 80 ± 5 mJ was measured, which is 60% of the incident energy. Therefore, 55 ± 5 mJ (40% of the incident energy) of the excimer laser pulse energy was absorbed at 760 torr by the plasma at the focal region. The energies absorbed by the plasma at different pressures such as 500 torr, 3 atm, and 5 atm are measured to be 48, 64, and 76 mJ, respectively, which correspond to 35%, 47%, and 56% of the incident energy, as expected with the increased laser absorption efficiency with pressure.

C. Plasma Spatial and Temporal Evolution

In order to understand the dynamical process of the laser-induced plasma and the time-resolved spatial distribution of the plasma and laser-heated neutral gas densities, we developed a laser shadowgraphy diagnostic technique [17]. In the plasma shadowgraphy technique, a synchronized CW probe laser beam is sent through the test section where the plasma is located and its image falls directly onto the ICCD with a 1 : 1 ratio on the image plane. If the refractive index in the test section μ is uniform, the screen will be essentially uniformly illuminated. If, however, the gradient of μ varies in space, as one may expect for high-density $(10^{14}-10^{18} cm^{-3})$ plasmas, i.e., when there is a significant second derivative of the refractive index, there will be variations in the illumination at the imaging screen. Regions where the second derivative of the refractive index is negative will act like a converging lens.

A comprehensive series of 15 shadowgrams is shown in Fig. 6, in which each image has a spatial extent of 1.3 cm $\times$ 1.3 cm. These shadowgrams show the spatial and temporal evolution of the laser-induced plasma obtained to measure the plasma volume, shock-wave velocities, and hot core air pressure. The observation was carried out in the horizontal direction, perpendicular to the axis of UV laser beam that is incident from the left. In Fig. 6, the laser beam propagates in the breakdown section toward the right along the z-axis. Positive z is measured from the focal spot toward the laser direction. Shadowgrams were obtained in the time span of a few nanoseconds to milliseconds. Time zero was defined as the leading edge of the laser pulse. Based on the shadowgraphy images, we observe that the plasma produced for separate laser shots is highly reproducible with very less variations due to the slight laser pulse energy fluctuations. A high bremsstrahlung emission was observed by means of a fast photodiode right
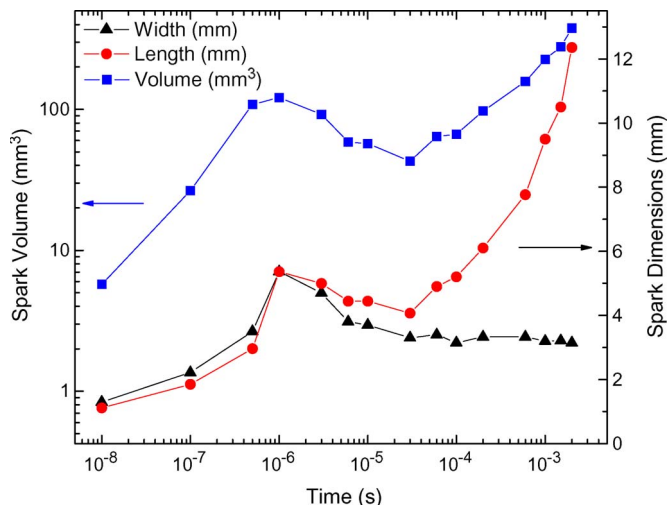
Fig. 7. Temporal evolution of the spatial characteristics (length, maximum width, and volume) of the laser-focused plasma for 135-mJ laser energy.

Fig. 8. Expansion of (circles) the shock and (squares) velocity of the shock front traveling against the incoming laser beam of 135 mJ.

after breakdown ($t < 25$ ns). For good shadowgram definition at $t = 10$ ns, the bremsstrahlung emission captured at a slightly earlier time ($t = 7$ ns) is subtracted. To achieve high-contrast images for 50 ns $< t <$ 100 μs, we have integrated 20 shots of the plasma produced during the expansion stage. For $t >$ 100 μs, single-shot images were recorded when the plasma became turbulent.

At very early times ($t \leq 100$ ns), the expansion of the heated region occurs, as a result of which the plasma takes on an asymmetrical shape along the z-axis with a clearly expressed sharper tip in the positive z-direction toward the incident laser. Here, time zero ($t = 0$) is considered to be the beginning of the laser pulse. After a certain time delay, the plasma reaches an electron density threshold such that the medium substantially absorbs the high laser flux powers of > 1 TW/cm^2, and thus, it expands out of the focal volume through a shock-wave mechanism [3]. At times up to 600 ns, the expanding plasma maintains a spherical shape with a slight oblateness in the z-direction. At ~ 1 μs, the neutral density shock wave separates from the hot core plasma due to gas heating with a more symmetrical spherical shape and continues to expand as clearly observed in the shadowgrams. Several wave propagation processes have been proposed to explain the plasma expansion phenomenon [3], [7]. It should be noted that each image is normalized by its maximum intensity value to preserve the detail, as the plasma and neutral density decay over time. The expanding shock wave is observed for times up to 60 μs. Later, the shock wave leaves the 1.3-cm × 1.3-cm field of view, followed by a sharp deformation of the irradiated region. It shows that the neutral density shock wave plays an important role for the stability of the hot core plasma expansion by enclosing it as a pressure barrier. The colder air around the focal point region penetrates the hot core air in the focal region, primarily in the z-direction. It causes the hot core air to expand and cool. The expansion causes the deformation of the hot core air into a structure of a vortex-type [17], [24] ring up to 2 ms; thereafter, the images available lose clarity. Fig. 7 shows that the size of the laser-induced plasma experiences rapid growth for the first 1 μs, after which, due to density decay processes and the penetration of
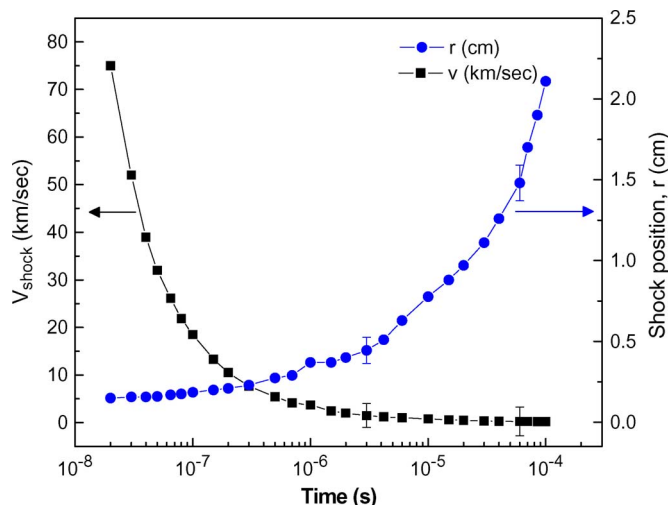
the cool air around the focal region into the hot core air, there is a reduction in plasma volume at around 20 μs. As observed in the shadowgrams, due to the irradiation and expansion gas dynamics discussed earlier, the hot core air deforms into a vortex torus shape and expands vertically, perpendicular to the z-direction (length), at a higher rate than along the z-axis (width), as shown in Fig. 7.

D. Electron Temperature Measurements

The shadowgraph images were used to measure the position and expansion velocity of the plasma and gas shock front. The position of the shock wave is measured from the focal point of the focusing lens group. Fig. 8 shows the radial position of the shock front, as well as the velocity of the plasma and gas shock as a function of time traveling toward the focusing optics, with an absorbed laser energy of 55 mJ at 760 torr. Based on the measurements and a numerical derivative of the measured position, the curve yields average velocities of 47 km/s, close to the values observed in longer wavelength laser plasma experiments [17]. Zeldovich and Raizer [18] have tabulated the flow quantities, primarily the temperature just behind a shock-wave front in air with standard conditions ahead of the wave ($p_0 = 1$ atm and $T_0 = 293$ K). Fig. 9 shows the temperature decay based on the measured velocities of the plasma and gas shock. We calculate the electron temperature behind the shock front approaching the value of 25 eV at $t = 10$ ns, and the temperature decays rapidly to 0.1 eV at 2 μs and continues to drop to 0.03 eV at 30 μs. These temperatures are comparable with those observed in longer wavelength (1.06-μm) laser focus air plasma experiments [17], [24].

IV. SUMMARY

The measurements of laser-induced breakdown threshold intensities for air using 193 nm and 180 mJ with a 20-ns pulsewidth excimer laser radiation for pressures ranging from 40 torr to 5 atm, where multi-photon and CC processes are significant, have been carried out. The measured breakdown
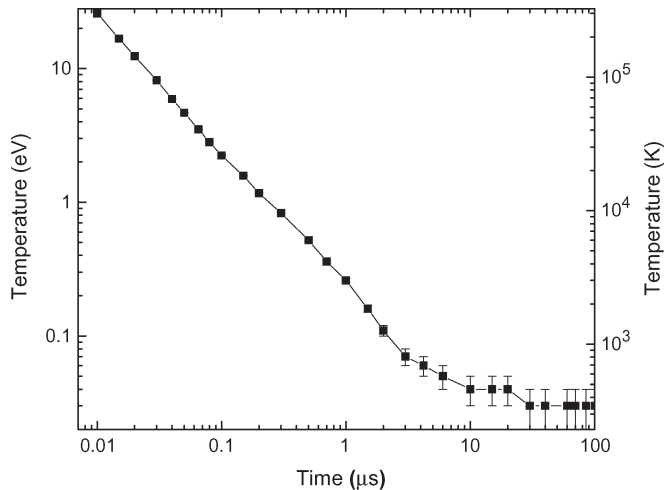
Fig. 9. Temperature decay of shock front as it expands out of the focal volume for 135-mJ laser pulse.

threshold field intensities are scaled to the classical microwave theory by correcting for MPI processes at various pressures. The MPI processes were observed to be dominant at pressures below 100 torr where the plasma is less collisional, whereas the cascade ionization process dominates for pressures above 100 torr up to 5 atm. Based on the breakdown measurements and comparing with the classical and quantum theories, 76% of the total ionization mechanism is carried out by the cascade ionization process, and 24% of the ionization process is carried out by the MPI process at $p = 760$ torr. At $p = 5$ atm, the highest pressure for which the pressure chamber was designed to operate and the breakdown threshold was measured, the MPI process is estimated to be 6%, and the cascade ionization process is estimated to be 94% of the total ionization process. At $p = 40$ torr, the lowest pressure at which the breakdown was measured in our experiment and the region is collisional, the MPI process is estimated to be 83%, and the cascade ionization process is 17% of the total ionization process. The MPI-corrected measured breakdown threshold data were scaled and fitted the CC microwave breakdown measurement pressure variation well. We also carried out 0.1-μm filtered measurements that somewhat increased the breakdown field at lower pressures in closer agreement with microwave measurements, indicating that small dust particles can enhance breakdown at short laser wavelengths.

For 135 ± 5-mJ laser incident energy at 760 torr, an average of 80 ± 5-mJ energy was measured to be transmitted through the plasma, which is 60% of the incident energy. Therefore, 55 ± 5 mJ (40% of the incident energy) of the excimer laser pulse energy was absorbed at 760 torr by the plasma at the focal region. The energies absorbed by the plasma, at different pressures such as 500 torr, 3 atm, and 5 atm, are measured to be 48, 64, and 76 mJ, respectively, which correspond to 35%, 47%, and 56% of the incident energy, as expected with the increased absorption efficiency with pressure.

The shadowgraphy diagnostics were performed to analyze the spatial and temporal evolution of the laser-induced plasma. Using this diagnostic on the plasma volume, shock-wave velocities were measured. An average shock-wave velocity of 47 km/s was measured from the expanding plasma and the laser-heated neutral shock wave. Based on the measured velocities of the plasma and gas shock, we calculate the electron temperature behind the shock front approaching values of 25 eV at $t = 10$ ns, and the temperature decays rapidly to 0.1 eV at 2 μs and continues to drop to 0.03 eV at 30 μs. This paper extends focused-laser dry-air breakdown experiments well into the UV regime where MPI effects substantially contribute to breakdown and plasma formation.

REFERENCES

[1] C. Phipps, *Laser Ablation and Its Applications*, 1st ed. New York: Springer-Verlag, 2006.
[2] C. A. David, *Lasers-Induced Plasmas and Applications*. Boca Raton, FL: CRC Press, 1989.
[3] Y. P. Raizer, *Gas Discharge Physics*. Berlin, Germany: Springer-Verlag, 1991.
[4] G. Bekefi, *Principles of Laser Plasmas*. New York: Wiley, 1976.
[5] M. P. Nelson, *C. R. Acad. Sci. Paris*, p. 259, 1964.
[6] N. Kroll and K. M. Watson, "Theoretical study of ionization of air by intense laser pulses," *Phys. Rev. A, Gen. Phys.*, vol. 5, no. 4, pp. 1883–1905, 1972.
[7] I. P. Shkarofsky, "Review of gas-breakdown phenomena induced by high-power lasers. I," *RCA Rev.*, vol. 35, pp. 48–78, Mar. 1974.
[8] C. H. Chan, C. D. Moody, and W. B. McKnight, "Significant loss mechanisms in gas breakdown at 10.6 μ," *J. Appl. Phys.*, vol. 44, no. 3, pp. 1179–1188, Mar. 1973.
[9] P. F. Browne, "Mechanism of gas breakdown by lasers," *Proc. Phys. Soc.*, vol. 86, no. 6, pp. 1323–1332, Dec. 1965.
[10] A. D. MacDonald, *Microwave Breakdown in Gases*. New York: Wiley, 1966.
[11] J. Stricker and J. G. Parker, "Experimental investigation of electrical breakdown in nitrogen and oxygen induced by focused laser radiation at 1.064 μ," *J. Appl. Phys.*, vol. 53, no. 2, pp. 851–855, Feb. 1982.
[12] A. A. Neuber, G. F. Edmiston, J. T. Krile, H. Krompholz, J. C. Dickens, and M. Kristiansen, "Interface breakdown during high-power microwave transmission," *IEEE Trans. Magn.*, vol. 43, no. 1, pp. 496–500, Jan. 2007.
[13] G. Edmiston, J. Krile, A. Neuber, J. Dickens, and H. Krompholz, "High-power microwave surface flashover of a gas–dielectric interface at 90–760 torr," *IEEE Trans. Plasma Sci.*, vol. 34, no. 5, pp. 1782–1788, Oct. 2006.
[14] E. M. Choi, M. A. Shapiro, J. R. Sirigiri, and R. J. Temkin, "Experimental study of a high efficiency 1.5 MW, 110 GHz gyrotron," in *Proc. IEEE Int. Vac. Electron. Conf.*, 2006, pp. 417–418.
[15] H. C. Kim and J. P. Verboncoeur, "Time-dependent physics of a single-surface multipactor discharge," *Phys. Plasmas*, vol. 12, no. 12, pp. 123 504-1–123 504-7, Dec. 2005.
[16] R. A. Kishek, Y. Y. Lau, L. K. Ang, A. Valfells, and R. M. Gilgenbach, "Multipactor discharge on metals and dielectrics: Historical review and recent theories," *Phys. Plasmas*, vol. 5, no. 5, p. 2120, May 1998.
[17] M. Villagran-Muniz, H. Sobral, and E. Camps, "Shadowgraphy and interferometry using a CW laser and a CCD of a laser-induced plasma in atmospheric air," *IEEE Trans. Plasma Sci.*, vol. 29, no. 4, pp. 613–616, Aug. 2001.
[18] Y. B. Zeldovich and Y. P. Raizer, *Physics of Shock Waves and High-Temperature Hydrodynamic Phenomena*, vol. 1. New York: Academic, 1966.
[19] S. Soubacq, P. Pignolet, E. Schall, and J. Batina, "Investigation of a gas breakdown process in a laser–plasma experiment," *J. Phys. D, Appl. Phys.*, vol. 37, no. 19, pp. 2686–2702, Sep. 2004.
[20] U. Jordan, D. Anderson, L. Lapierre, M. Lisak, T. Olsson, J. Puech, V. E. Semenov, J. Sombrin, and R. Tomala, "On the effective diffusion length for microwave breakdown," *IEEE Trans. Plasma Sci.*, vol. 34, no. 2, pp. 421–430, Apr. 2006.
[21] K. H. Becker, U. Kogelschatz, K. H. Schoenbach, and R. J. Barker, *Non-Equilibrium Air Plasmas at Atmospheric Pressure*. Bristol, U.K.: Inst. Phys. Publ., 2005.

[22] R. Tambay and R. K. Thareja, "Laser-induced breakdown studies of laboratory air at 0.266, 0.355, 0.532, and 1.06 μm," *J. Appl. Phys.*, vol. 70, no. 5, pp. 2890–2892, 1991.

[23] D. E. Lencioni and L. C. Pettingill, "The dynamics of air breakdown initiated by a particle in a laser beam," *J. Appl. Phys.*, vol. 48, no. 5, pp. 1848–1851, May 1977.

[24] M. Villagran-Muniz, H. Sobral, and R. Navarro-Gonzalez, "Shock and thermal wave study of laser-induced plasmas in air by the probe beam deflection technique," *Meas. Sci. Technol.*, vol. 14, no. 5, pp. 614–618, Mar. 2003.

Magesh Thiyagarajan (M'01) received the B.E. degree in electrical and electronics engineering (with honors) from the University of Madras, Chennai, India, in 2001, the M.S. degree in (plasmas) electrical engineering (with the citation for professional promise) from the University of Tennessee, Knoxville, in 2004, and the Ph.D. degree in (plasma physics) electrical engineering from the University of Wisconsin, Madison, in 2007.

Currently, he is a Scientist with the General Electric—Global Research Center, Niskayuna, NY. During his work at Tennessee, he researched nonthermal atmospheric-pressure large-volume plasmas, plasma-biological sterilization, plasma-chemical decontamination, tunable plasma stealth antennas, and plasma ball lightning. During his work at Wisconsin, he researched UV-laser-focused plasmas, UV-laser-induced RF inductively coupled plasmas, laser shadowgraphy, laser and microwave interferometry, and optical emission spectroscopy. His current research interests include plasma waste gasification, plasma torches, spectroscopy, plasma medicine, and holographic data storage.

Dr. Thiyagarajan received the Best New Technology Business Award from the Wisconsin governor in 2006 and the IEEE Graduate Student Scholarship Award in 2004. He was the Vice President of the IEEE Chapter, Wisconsin—Madison (2004–2005). He is an active member of the engineering honor societies of Tau Beta Pi, Eta Kappa Nu, and Order of the Engineer.

John E. Scharer (SM'90) received the B.S., M.S., and Ph.D. degrees in electrical engineering and plasma physics from the University of California, Berkeley.

He is a Professor with the Department of Electrical and Computer Engineering and the Codirector of the Center for Plasma Theory and Computation, University of Wisconsin, Madison. He spent sabbaticals at the Commissariat a l'Energie Atomique, Fontenary-aux-Roses, France, in 1970, the Joint European Torus, Culham, U.K., in 1983, and the Australian National University, Sydney, Australia, in 2000, working on RF plasma physics. He has substantial research experience in excimer-laser–plasma creation, optical spectroscopy, radio-frequency sustainment, millimeter-wave diagnostics, and chemistry of organic seed gas plasmas in air and microwave vacuum electronics. He also has extensive experience in theoretical, computational, and experimental research works on antenna coupling and wave propagation, as well as heating and creative diagnostics in plasmas and vacuum electronics.